



PATENT
SD7566S103423

IN THE UNITED STATES PATENT AND TRADEMARK OFFICE

In re application of: Vawter et al

Group No.: 2877

Serial No.: 10/ 780,799

Examiner: Turner, S.

Filed: February 17, 2004

For: Integrated Resonant Micro-Optical Gyroscope and Method of Fabrication

Commissioner for Patents

P.O. Box 1450

Alexandria, VA 22313-1450

**DECLARATION REGARDING INVENTORSHIP UNDER 37 CFR 1.132 TO
OVERCOME CITED REFERENCE BY Vawter et al**

PURPOSE OF DECLARATION

This declaration is to establish that a reference cited as Vawter et al in the 35 U.S.C. 102(a) and 103(a) rejections in the First Office Action of February 23, 2006 (Paper No. 021706) and attached hereto as Exhibit A describes Applicants' own work, and is the publication of Applicants' own invention.

The persons making this declaration are co-inventors of the above referenced patent application and co-authors of the Vawter et al reference.

REVIEW OF CIRCUMSTANCES

Claims 1, 4, 7, 9-13, 15, 18-20, 22, 23, 25-32, 36, 38 and 39 have been rejected under 35 U. S. C. §102(a) as being anticipated in view of the following reference cited as Vawter et al which was presented within one year of Applicants filing date:

Vawter et al., *Developments in Pursuit of a Micro-Optic Gyroscope*, Sandia National Laboratories Report No. SAND2003-0665, March 2003.

Claims 2, 3, 6, 8, 21 and 37 have been rejected under 35 U. S. C. §103(a) as being obvious in view of a combination of references including the above Vawter et al reference.

FACTS

The authorship heading of the Vawter et al reference enclosed herewith lists co-authors G. Allen Vawter, Walter J. Zubrzycki, James J. Hudgens, Gregory M. Peake, Charles Alford, Terry Hargett, Betty Salters and Ragon D. Kinney as being affiliated with Sandia National Laboratories at the time the work described therein was performed. Co-authors G. Allen Vawter and Walter J. Zubrzycki of the above Vawter et al reference are also co-inventors of the same names for the referenced patent application disclosing and claiming the invention which is included in the Vawter et al reference.

James J. Hudgens, Gregory M. Peake, Charles Alford, Terry Hargett, Betty Salters and Ragon D. Kinney are listed as co-authors of the above reference, but are not co-inventors of the referenced patent application disclosing and claiming the invention which is included in the Vawter et al reference.

Junpeng Guo and Charles T. Sullivan are co-inventors of the referenced patent application disclosing and claiming the invention which is included in the Vawter et al reference, but are not listed as co-authors on the Vawter et al reference.

TIME OF PRESENTATION OF THE DECLARATION

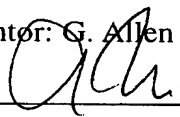
This declaration is submitted prior to final rejection.

DECLARATION

1. I hereby declare that I am a co-author of the above reference cited as Vawter et al.
2. I hereby further declare that the Vawter et al reference describes my own work and the invention for which the patent application referenced herein has been submitted, and of which I am a co-inventor.
3. I hereby declare that James J. Hudgens, Gregory M. Peake, Charles Alford, Terry Hargett, Betty Salters and Ragon D. Kinney, although listed as co-authors of the Vawter et al reference, are not co-inventors of the patent application referenced herein.
4. I hereby declare that Junpeng Guo and Charles T. Sullivan, although not listed as co-authors of the Vawter et al reference, are co-inventors of the patent application referenced herein.
5. I hereby declare that all statements made herein of my own knowledge are true, and that all statements made on information and belief are believed to be true; and further that these statements were made with the knowledge that willful false statements and the like so made are punishable by fine or imprisonment, or both, under Section 1001 of Title 18 of the United States Code, and that such willful false statements may jeopardize the validity of the patent application or any patent issued thereon.

SIGNATURES

Full name of co-inventor: G. Allen Vawter

Inventor's signature: 

Date: 3/28/06

Citizenship: U. S. A.

Residence: Corrales, New Mexico 87048

Post Office Address: 111 Mission Ridge, Corrales, New Mexico 87048

Patent - Serial # 10/ 780,799
SD7566S103423
Page 3

Full name of co-inventor: Walter J. Zubrzycki

Inventor's signature: Walter J. Zubrzycki

Date: 3/28/2006

Citizenship: U. S. A.

Residence: Sandia Park, New Mexico 87047

Post Office Address: 56 Vista Bonita Drive, Sandia Park, New Mexico 87047



Exhibit A

SAND REPORT

SAND2003-0665
Unlimited Release
Printed March 2003

Developments in Pursuit of a Micro-Optic Gyroscope

G. Allen Vawter, Walter J. Zubrzycki, James J. Hudgens, Gregory M. Peake, Charles Alford, Terry Hargett, Betty Salters, and Ragon D. Kinney

Prepared by
Sandia National Laboratories
Albuquerque, New Mexico 87185 and Livermore, California 94550

Sandia is a multiprogram laboratory operated by Sandia Corporation, a Lockheed Martin Company, for the United States Department of Energy's National Nuclear Security Administration under Contract DE-AC04-94-AL85000.

Approved for public release; further dissemination unlimited.



Sandia National Laboratories

Issued by Sandia National Laboratories, operated for the United States Department of Energy by Sandia Corporation.

NOTICE: This report was prepared as an account of work sponsored by an agency of the United States Government. Neither the United States Government, nor any agency thereof, nor any of their employees, nor any of their contractors, subcontractors, or their employees, make any warranty, express or implied, or assume any legal liability or responsibility for the accuracy, completeness, or usefulness of any information, apparatus, product, or process disclosed, or represent that its use would not infringe privately owned rights. Reference herein to any specific commercial product, process, or service by trade name, trademark, manufacturer, or otherwise, does not necessarily constitute or imply its endorsement, recommendation, or favoring by the United States Government, any agency thereof, or any of their contractors or subcontractors. The views and opinions expressed herein do not necessarily state or reflect those of the United States Government, any agency thereof, or any of their contractors.

Printed in the United States of America. This report has been reproduced directly from the best available copy.

Available to DOE and DOE contractors from
U.S. Department of Energy
Office of Scientific and Technical Information
P.O. Box 62
Oak Ridge, TN 37831

Telephone: (865)576-8401
Facsimile: (865)576-5728
E-Mail: reports@adonis.osti.gov
Online ordering: <http://www.doe.gov/bridge>

Available to the public from
U.S. Department of Commerce
National Technical Information Service
5285 Port Royal Rd
Springfield, VA 22161

Telephone: (800)553-6847
Facsimile: (703)605-6900
E-Mail: orders@ntis.fedworld.gov
Online order: <http://www.ntis.gov/help/ordermethods.asp?loc=7-4-0#online>



SAND2003-0665
Unlimited Release
Printed March 2003

Developments in Pursuit of a Micro-Optic Gyroscope

**G. Allen Vawter, Walter J. Zubrzycki, Gregory M. Peake,
Charles Alford, Terry Hargett, and Betty Salters
RF Microsystems Technologies**

**James J. Hudgens
Integrated Microsystems**

**Ragon D. Kinney
Inertial Systems**

**Sandia National Laboratories
PO Box 5800
Albuquerque, NM 87185-0501**

Abstract

Rotation sensors (gyros) and accelerometers are essential components for all precision-guided weapons and autonomous mobile surveillance platforms. MEMS gyro development has been based primarily on the properties of moving mass to sense rotation and has failed to keep pace with the concurrent development of MEMS accelerometers because the reduction of size and therefore mass is substantially more detrimental to the performance of gyros than to accelerometers.

A small (~0.2 cu in), robust (~20,000g), inexpensive (~\$500), tactical grade performance (~10-20 deg/hr.) gyro is vital for the successful implementation of the next generation of "smart" weapons and surveillance apparatus. The range of applications (relevant to Sandia's mission) that are substantially enhanced in capability or enabled by the availability of a gyro possessing the above attributes includes nuclear weapon guidance, fuzing, and safing; synthetic aperture radar (SAR) motion compensation; autonomous air and ground vehicles; gun-launched munitions; satellite control; and personnel tracking. For example, a gyro of this capability would open for consideration more fuzing options for earth-penetration weapons.

The MEMS gyros currently available are lacking in one or more of the aforementioned attributes. An integrated optical gyro, however, possesses the potential of achieving all desired attributes. Optical gyros use the properties of light to sense rotation and require no moving mass. Only the individual optical elements required for the generation, detection, and control of light are susceptible to shock. Integrating these elements immensely enhances the gyro's robustness while achieving size and cost reduction.

This project's goal, a joint effort between organizations 2300 and 1700, was to demonstrate an RMOG produced from a monolithic photonic integrated circuit coupled with a SiON waveguide resonator. During this LDRD program, we have developed the photonic elements necessary for a resonant micro-optical gyro. We individually designed an AlGaAs distributed Bragg reflector laser; GaAs phase modulator and GaAs photodiode detector. Furthermore, we have fabricated a breadboard gyroscope, which was used to confirm modeling and evaluate signal processing and control circuits.

TABLE OF CONTENTS

Developments in Pursuit of a Micro-Optic Gyroscope.....	I
1. PURSUIT OF A MICRO-OPTIC GYRO: THE MOTIVATION	7
1.1. Environmental Sensing Devices in Nuclear Weapons-An Overview	7
1.2. Gyros in Nuclear Weapons-Why Their Absence?	7
1.3. New Developments in Inertial Sensors Provide New Options	8
1.4. Disparity in the Advances of MEMS Accelerometers and Gyros	8
1.5. Current Status of MEMS Gyros.....	9
1.6. MEMS Gyros in Nuclear Weapons-An Assessment of Requirements.....	10
1.7. The Micro-Optic Gyro-A Different Approach.....	11
2. BASIC GYRO TECHNOLOGY	11
2.1. Introduction.....	11
2.1.1. Sagnac Effect.....	11
2.1.2. Kerr Effects	19
2.1.3. Stress Birefringence.....	20
2.1.4. Rayleigh Scattering.....	20
2.2. Signal Processing.....	21
2.2.1. Biasing.....	21
2.2.2. Closed Loop Operation	21
3. GYRO BREADBOARD	22
3.1. Purpose.....	22
3.2. Breadboard Design	22

3.3.	Breadboard Components and Configuration.....	24
3.4.	Experimentation Using the Breadboard.....	25
3.5.	Future Work.....	29
4.	HYBRID PHOTONIC APPROACH.....	29
4.1.	Development of the Semiconductor PIC Components	30
4.2.	Design Criteria	31
4.3.	Progress towards Component Realization.....	32
4.3.1.	AlGaAs DFB laser for photonic integrated circuits.....	32
4.3.2.	Active/passive integration technology based on selective-area disordering ...	33
4.3.3.	Active-Passive Integration Progress.....	34
4.3.4.	Experimental Evaluation of Disordered Components.....	35
5.	SUMMARY OF ACCOMPLISHMENTS.....	36
6.	APPENDIX A.....	38
7.	DISTRIBUTION	39

1. Pursuit of a Micro-Optic Gyro: The Motivation

1.1. Environmental Sensing Devices in Nuclear Weapons-An Overview

Environment sensing devices (ESD) have always played an important role in nuclear weapon systems predominantly in components used in the safety architecture. These devices have been fundamental to implementing a safety theme based on detecting the presence of certain characteristics of the weapon's dynamical environment following deployment from the carrier vehicle—such as its roll-rate or acceleration profile or both—as a precondition to arming the weapon.

The typical ESD residing in our nuclear stockpile today is a “g-switch,” a device designed to change its state from “off” to “on” whenever the acceleration acting along a selected axis of its host vehicle exceeds a specific level or in another variant, when an acceleration-time product is exceeded. Rotational velocities are detected by sensing the centrifugal accelerations generated at select locations in the spinning weapon. In either event, the most information available from a g-switch is whether the weapon exceeded a particular threshold of acceleration or g-second product.

The g-switch employed in weapons in the current stockpile is the Rolamite, an entirely mechanical mechanism typically consisting of two cylindrical metal rollers interconnected with a thin metal band housed in a sealed enclosure that is sometimes filled with a fluid to implement an integration of the input acceleration.

1.2. Gyros in Nuclear Weapons-Why Their Absence?

The low utilization of gyroscopes in nuclear weapons is, at first glance, surprising, especially considering the many attractive attributes these devices possess. It is clear that the most rudimentary of gyroscopes offers the designer a superior instrument for measuring bomb rotational velocities than, for example, the g-switch (Rolamite) typically used to detect such environments. Unfortunately, the design decisions underlying this absence are not well documented. One can, however, draw some reasonable hypotheses based on the known weaknesses of early gyro designs.

Intricate designs consisting of precision bearings, rotors, electric spin motors, and floats with bellows for temperature compensation were characteristics of early gyros. Design complexity is frequently perceived as being synonymous with low reliability, a legitimate perception of early vintage gyros, which frequently manifested a poor mean time to failure.

Sensor cost may have been a precluding driver in some designs, although, in general, this is unlikely since cost was less a priority in previous years than it is today.

Unfamiliarity of the weapon engineer with inertial instruments was probably a contributing factor. The early years of nuclear weapon development coincided with the genesis of inertial guidance. Training in inertial measurement sensors was spotty and this conceivably resulted in solutions to environment sensing problems being implemented in more familiar but less optimal ways.

Susceptibility to ionizing radiation was and remains a major concern for inertial sensors containing electronic components. G-switches in the genre of the Rolamite are inherently

hard to ionizing radiation and this attribute alone can be sufficient to sway a designer to decide in favor of a g-switch approach despite the fact that such a selection is significantly less than optimal in addressing certain requirements such as detecting bomb roll-rate.

Probably the dominant reason for low utilization was the steadfast pursuit of a safety theme based on excluding devices requiring electrical energy for operation from selected parts of the arming signal path. This undoubtedly eliminated most precision inertial sensors from consideration for use in the safety architecture of the weapon. This continues to be a valid concern. Few, if any, inertial instruments that are available today come without some electrical interface. However, this does not account for the lack of such devices in other areas of the weapon architecture such as fuzing and controlling weapon orientation.

It should be noted that, though rare in number, there have been some noteworthy examples of the use of precision inertial sensors in nuclear weapons. For instance, a high-precision integrating forced-balanced accelerometer was used in the fuze design of the W88 warhead and the B77 bomb designers used a rate gyroscope in the roll-control system of the bomb.

1.3. New Developments in Inertial Sensors Provide New Options

The more recent developments of optical rotation sensors, ring-laser and fiber-optic gyros, and silicon-based micro machined electromechanical systems (MEMS) inertial sensors mitigate many of the deficiencies of earlier technologies and provide today's weapon designer with broader options.

For example, using the properties of light to sense rotation provides the basis for implementing rotation sensors with no moving parts and practically instant activation time. The former attribute enhances prospects for realizing sensors that can remain dormant for many years in the stockpile and still work reliably when called to do so. The latter removes the time requirement for activating the sensing element of the gyroscope—not an insignificant attribute considering that weapons are often kept in an unpowered state until the last stage of deployment.

MEMS-based sensor designs that integrate the electronics with the sensing element provide a sensor technology possessing dramatically lower cost, size, weight, and power together with enhanced functionality compared to g-switches and essentially no sacrifice in reliability. In fact, overall system reliability can potentially be improved through redundancy of selected subsystems while incurring only a minimal penalty in cost, weight, and volume.

1.4. Disparity in the Advances of MEMS Accelerometers and Gyros

A poster child for MEMS inertial sensor technology and one displaying all the attributes of low cost, small size, and weight, and low power mentioned previously is Analog Devices, Inc (ADI) highly successful MEMS accelerometer family that is presently being produced at a rate of over one million devices per month. One version, the ADXL202E, is a two-axis accelerometer consisting of two independent sensing structures and all their signal conditioning electronics integrated on a single silicon chip and packaged in a five-millimeter square, two-millimeter thick, leadless chip carrier that sells in large quantities for less than \$9.00. The price includes the cost of 100% testing of each device over a

temperature range of -40°C to $+125^{\circ}\text{C}$. Of particular significance to nuclear weapon designers, failure rates of production devices are reported to be less than 5 parts per million¹.

Unfortunately, MEMS gyroscope developments to date have not achieved the same level of success as MEMS accelerometers. Arguably, this can be attributed to the preference of researchers for gyro designs based on the properties of moving mass. The typical MEMS gyro available today measures rotation by detecting the Coriolis forces acting on vibratory mechanical structures in the presence of rotation. The problem with this approach is that in pursuing reduced sensor size one must also contend with the resultant reduction in sense element's mass and this is not compatible with achieving good performance, but most significantly, the reduction in mass is substantially more detrimental to the performance of gyros than to accelerometers. The difference in degree of difficulty in implementing the two sensor types as MEMS devices is clearly evident in the fact that Analog Devices introduced their first MEMS gyroscope and the world's first totally integrated MEMS production gyroscope, the ADXRS150, in October 2002.

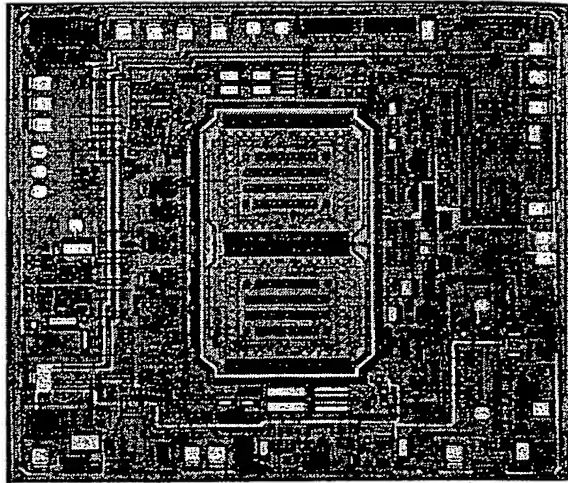


Figure 1 ADXRS 150 MEMS Gyro Showing Rate Sensors and Integrated Electronics

1.5. Current Status of MEMS Gyros

Table 1 provides a comparison of three commercial-off-the-shelf (COTS) MEMS gyros with the ADXRS150 being representative of the most recent advances in the technology. The listing is not exhaustive but is representative of the state of the art at this time. Worth noting is the fact that of the gyros listed in Table 1 only the Analog Devices' gyro is fully integrated. In the other designs, the vibratory structure is fabricated on a substrate separate from the electronics. This is typical and although this approach allows the fabrication of larger and more massive sensing structures, it increases the sensor's electrical noise and presents obstacles for achieving environmental robustness.

Table 1 Published attributes for three state-of-the-art COTS MEMS gyroscopes

COTS MEMS Gyro	Size mm ²	Rate Range deg/s	Short Term Bias Stability deg/hr	Bias Temp Coefficient deg/hr/°C	Scale Factor TC %/°C	Nonlinearity % of Full Scale	Bandwidth Hz	Noise deg/hr/Hz ^{1/2}	G sensitivity deg/hr/g	Operating Temp Range deg C	Shock Capability g @ ms 1/2 sine
ADXRS150	150	±150	180	440	±0.04	0.1	500	180	720	-40—85	1000/0.5
SiRRS01	17275	±110	3	111	±0.05	1	50	127	7	-40—75	60/30
QRS11	15346	±100	7	20	±0.03	0.05	60	108	72	-40—80	200/na

¹ telephone conversation with Harvey Weinberg, ADI application engineer, October 2002

Figure 2 Silicon Sensing Systems' SiSSR01
Vibratory Gyro

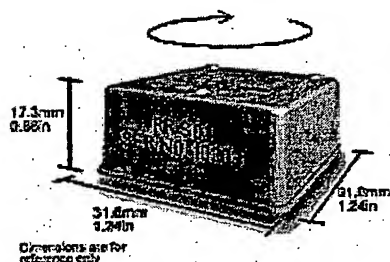
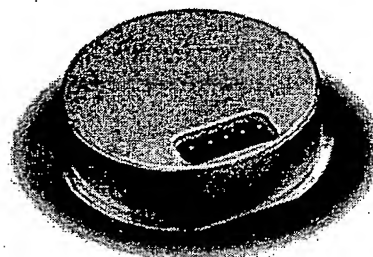


Figure 3 BEI Angular Rate
Sensor, QRS11



Two U.S. government-funded programs, a joint Army/Navy development² and a Defense Advanced Research Project Agency (DARPA) initiative³, are currently in progress to develop MEMS-based inertial measurement units (IMU). If the goals of either development effort are met, a MEMS-based IMU possessing drift performance on the order of 1-10 degree/hour will be realized. Most likely, however, this level of performance will be achieved only through software compensation of the individual sensors at the system level and therefore may not produce a standalone MEMS gyro of this performance level.

It is well publicized⁴ that a participant in the join Army/Navy development, Honeywell, International, is continuing the refinement of a vibratory MEMS gyro design initially conceived by Draper Laboratory and it is not unreasonable to assume that the other participants are also pursuing silicon vibratory gyros.

1.6. MEMS Gyros in Nuclear Weapons-An Assessment of Requirements

To date, environmental sensing requirements for nuclear weapons have not required a gyro of 1 degree/hour bias stability, but the availability of a small (~0.2 cu in), robust (~20,000g), inexpensive (~\$500), tactical performance (~20 deg/hr drift.), gyro capable of dwelling dormant in long-term (20 years) storage and operating within specification without benefit of calibration would substantially enhance the prospects of realizing several use scenarios for the next generation nuclear weapon. The realization of such a gyro would, for example, expand the fuzing options available to the designers of an earth-penetrating weapon. If the aforementioned military-funded development programs are successful, perhaps a standalone MEMS vibratory gyro possessing the desired attributes will be available. However, based on Sandia's experience derived from participation in vibratory gyro developments at the University of California at Berkeley and to lesser degree via a cooperative research and development agreement (CRADA) with Northrop-

² Broad Agency Announcement (BAA), DAA30-01-BAA-0101, March 2001

³ reference web site: <http://www.darpa.mil/spo/programs/memsins.htm> and Appendix A

⁴ Mueller, Conrad, "Inertial Measurement Unit Production Evolution: from Ring Laser Gyros to Fiber Optic Gyros to MicroElectroMechanical Systems," Defense Manufacturing Conference presentation, November 30, 1999

Grumman (formerly Litton Guidance and Control System), it is not at all clear that either program can succeed via a vibratory gyro.

1.7. The Micro-Optic Gyro-A Different Approach

There is another path to MEMS gyro realization, the integrated micro-optic gyro, which has been previously proposed⁵ but not consistently pursued with the depth of effort necessary to fully exploit the technology. This was most probably a consequence of the requisite technologies in photonics lacking maturity and partly because the resources to pursue this endeavor along all paths necessary to achieve a fully integrated gyro were not available within one organization.

An integrated micro-optical gyro, the building blocks of which were pursued in this LDRD, has the potential of achieving many attributes attractive to the nuclear weapon designer. Only the individual optical elements necessary for the generation, detection, control, and containment of light are susceptible to shock. Integrating these elements into a common substrate immensely enhances the gyro's robustness and its reliability while concurrently achieving size, cost, and power reduction.

The work described in this report addresses different facets of the design problem each of which could be pursued at this stage independently of the others without compromising the ultimate goal. Reported in this document are the details of an error model, which proved essential in providing the values for various design parameters and used to guide development of the integrated optical components, the efforts in active/passive integration of key photonic components, the design of the laser light source, and the design of a solid state optical waveguide.

2. Basic Gyro Technology

2.1. Introduction

In this section we will give an overview of the basic principles of operation of fiber optic gyroscopes. We discuss the Sagnac effect and then review two types of passive Sagnac interferometers, the interferometric fiber optic interferometer and the resonant fiber optic interferometer. Several error sources such as the Kerr effect, stress birefringence, and Rayleigh scattering are also discussed.

2.1.1. Sagnac Effect

Whereas mechanical gyroscopes are based on the conservation of momentum in a frame of reference fixed in the stars, optical gyroscopes are based on the inertial property of light. All optical gyros use the Sagnac effect to measure rotation^{6, 7, 8, 9, 10}. Though the

⁵ Lawrence, A.W., "Thin film Laser Gyro," U.S. Patent 4 326 803, 27 April 1982

⁶ William K. Burns, editor. *Optical Rotation Sensing*. Academic Press Inc., San Diego, CA, 1994.

⁷ B. Yoon Kim and Herbert John Shaw. Fiber-optic gyroscopes. *IEEE Spectrum*, pages 54-60, March 1986.

⁸ D.A. Krohn. *Fiber Optic Sensors: Fundamentals and Applications*. Instrument Society of America, Research Triangle Park, NC, 1992.

⁹ Herve Lefevre. *The Fiber-Optic Gyroscope*. Artech House, Boston, 1993.

¹⁰ R.E. Meyer, S. Exekiel, D.W. Stowe and V.J. Tekippe. Passive fiber-optic ring resonator for rotation sensing. *Optics Letters*, 8(12): 644-646, December 1983.

general theory of relativity must be used to perform the exact calculation of the Sagnac effect the description in what follows is sufficient here.

Consider the case in Figure 4 where a platform is rotating with angular rate Ω (assume the light is traveling in free space). At time $t_0=0$ light is sent in both the clockwise (cw) and counter clockwise (ccw) directions in a circular path. The distance traveled by the cw path is given by

$$L_{cw} = 2\pi R - R\Omega t_{cw} \quad (1)$$

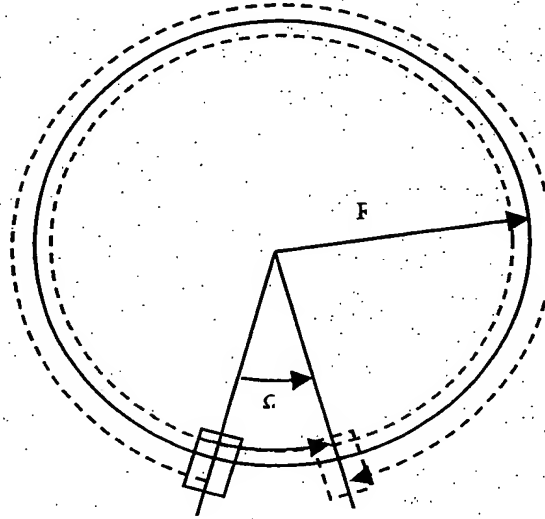
While the ccw path is

$$L_{ccw} = 2\pi R + R\Omega t_{ccw} \quad (2)$$

Where R is the radius of the circular path. The difference in time for each path is

$$\Delta t = t_{ccw} - t_{cw} = \frac{L_{ccw}}{c} - \frac{L_{cw}}{c} = \frac{R\Omega(t_{cw} + t_{ccw})}{c} = \frac{R\Omega(2\pi R + 2\pi R)}{c^2} = \frac{4A\Omega}{c^2} \quad (3)$$

Figure 4 Time difference due to the Sagnac effect



where c is the speed of light and A is the area of the optical path.

The effective change in length for the optical paths is thus given by

$$\Delta L = \frac{4A\Omega}{c} \quad (4)$$

Assuming an optical path area of $A=100\text{cm}^2$ and a rotation rate $\Omega = 1\text{rad/sec}$ we get a ΔL of $1.3 \times 10^{-8}\text{ cm}$. Tactical grade inertial navigation requires rotation rate to be measured at an accuracy of $<1\text{deg/hr}$ or $<4.8 \times 10^{-6}\text{ rad/sec}$. Therefore, ΔL must be measured to $<1 \times 10^{-13}\text{ cm}$. Both active and passive interferometric methods have been used to measure such small ΔL 's. Multiple beam Fabry-Perot interferometers and single beam Mach-Zender type interferometers have been utilized. An open loop interferometric fiber optic gyroscope (IFOG) is shown in Figure 5. The

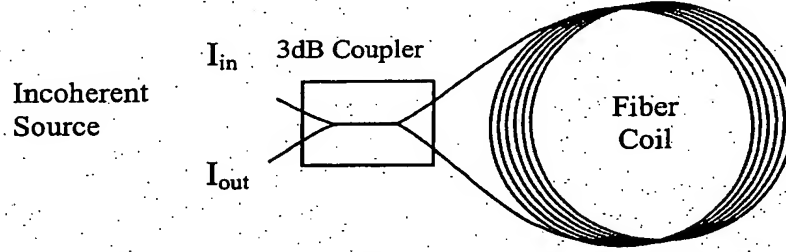


Figure 5 A basic open loop Interferometric gyroscope

IFOG is a common path interferometer. The input light is split by a 3dB fiber coupler and the light travels in opposite directions around the common fiber loop. After a single trip around the fiber loop the light then recombines at the fiber coupler and 50% of the resulting intensity is detected at I_{out} . An applied angular rotation rate normal to the plane of the interferometer will result in a phase shift between the cw and ccw propagating beams. The magnitude of the phase shift, $\Delta\phi$, is given by:

$$\Delta\phi = \frac{2\pi}{\lambda_0} \Delta L = \frac{8\pi A}{\lambda_0 c_0} \Omega \quad (5)$$

where λ_0 is the wavelength of light in a vacuum. The output intensity of the interferometer is cosinusoidal as a function of Ω . The use of a fiber interferometer enables the loop to be coiled N times. In this way the sensitivity of the interferometer is increased by a factor of N as given by:

$$\Delta\phi_f = \frac{8\pi AN}{\lambda_0 c_0} \Omega = \frac{L_f D}{c_0} \Omega \quad (6)$$

where L_f is the length of fiber in the loop and D is the diameter of the fiber loop.

For an optical gyroscope to work accurately it must have perfect optical reciprocity. For the configuration shown in Figure 5, the light along the cw path is reflected twice by the coupler while the light in the ccw path will be transmitted twice by the coupler. Differences in transmission and coupler introduce

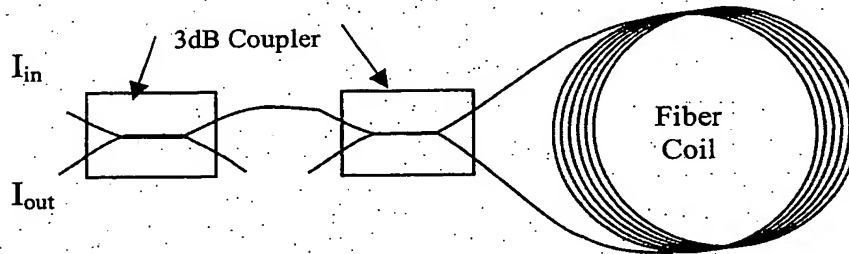


Figure 6 The minimum configuration

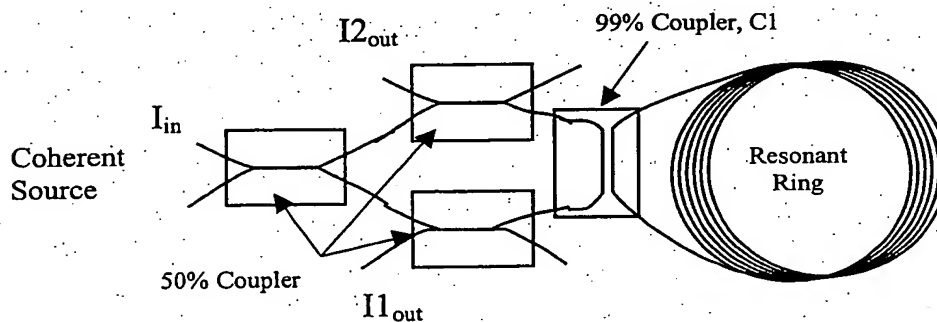
phase conditions for reflection of the non-reciprocity. A

fully reciprocal IFOG design is shown in Figure 6. This design is referred to as the minimum configuration for an IFOG and both the cw and ccw paths undergo the same number of reflections and transmissions at the couplers.

Whereas the IFOG is analogous to a Mach-Zender interferometer, an RFOG is like a Fabry-Perot type interferometer where the light circulates in the cavity many times. The layout of a basic RFOG is shown in Figure 7.

The light from each path in the RFOG enters a coupler (typically on the order of 99 to 1) which transfers some of the light into the resonator loop as shown in Figure 7. Once inside the light travels repeatedly around the resonator losing energy due to the lossy medium and the couplers. When the light travels many times around the path, the resulting intensity leaving the coupler depends upon the interference of light having circulated within the resonator various times.

Figure 7 Basic RFOG operated in reflection



The field transmission coefficient τ_i represents the amplitude transmitted to the resonator, while τ_i' is the field transmission constant out of the resonator for the i^{th} coupler^{11,12}. The

¹¹ Max Born and Emil Wolf. *Principles of Optics: Electromagnetic Theory of Propagation, Interference and Diffraction of Light*. Pergamon Press, Oxford, fifth edition, 1975.

¹² Jurgen R. Meyer-Arendt. *Introduction to Classical and Modern Optics*. Prentice Hall, Englewood Cliffs, NJ, third edition, 1998.

field rejection coefficient ρ_i is used outside the resonator, while ρ_i' is the field transmission constant within the resonator. We will assume that the wave guide has a field attenuation of α per unit length due to fiber losses.

Assume that the field reaching coupler, C1, (refer to Figure 7) is given by $Ae^{j\omega t}$. Then the amplitude just within the resonator is given by $B_0 = \tau_1 Ae^{j\omega t}$, while the amplitude passed to the detector is $\rho_1 Ae^{j\omega t}$. The light within the resonator will continue to circulate losing amplitude due to the fiber optic material and coupler. Assume that during each pass around the resonator that the phase difference between successive passes is δ . The field in the resonator at the output of coupler, C1, will be

$$\begin{aligned} B_0 &= \tau_1 Ae^{j\omega t} \\ B_1 &= \tau_1 A \rho_1' e^{[j(\omega t + \delta) - \alpha L]} \\ B_2 &= \tau_1 A \rho_1'^2 e^{[j(\omega t + 2\delta) - 2\alpha L]} \end{aligned} \quad (7)$$

Where B_k is the field after circulating k times.

The field at the output of the resonator becomes

$$E_0 = \rho_1 Ae^{j\omega t} + \tau_1 \tau_1' A \rho_1' e^{[j(\omega t + \delta) - \alpha L]} \sum_{k=0}^{\infty} \rho_1'^k e^{k[j\delta - \alpha L]} \quad (8)$$

Given

$$\sum_{k=0}^{\infty} a^k = \frac{1}{1-a} \quad (9)$$

for any a with $|a| < 1$, we find

$$E_0 = A \left[\rho_1 + \frac{T e^{(j\delta - \alpha L)}}{1 - \rho_1' e^{(j\delta - \alpha L)}} \right] e^{j\omega t}, \quad (10)$$

where $T = \tau_1 \tau_1'$. Since the input field at the resonator is $E_i = Ae^{j\omega t}$, the input-output power ratio becomes

$$\frac{P_0}{P_i} = \frac{E_0^* E_0}{E_i^* E_i} \quad (11)$$

where $*$ denotes the complex conjugate. Figure 8 shows the resonator response as a function of frequency. Notice the response is much sharper than the cosine response of the IFOG. The width of the response is affected by the coupler reflection coefficient and fiber loss. The width of the response is quantified by the finesse.

The finesse is defined as

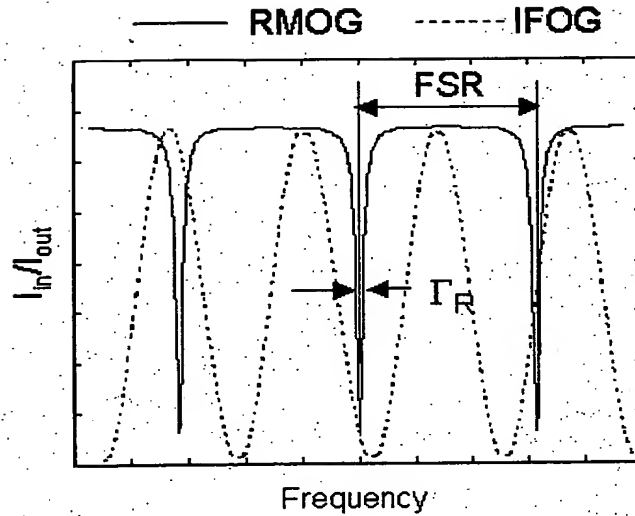


Figure 8 A comparison of the intensity response of an RFOG and IFOG where FSR is the free spectral range and Γ_R is the resonator linewidth

$$F = \frac{f_{sr}}{\Gamma_R + \Gamma_{laser}} \quad (12)$$

where f_{sr} is the free spectral range, Γ_R is the resonator linewidth, and Γ_{laser} is the linewidth of the laser. Therefore, the laser linewidth must be much less than the resonator linewidth. Practically, the laser linewidth must be less than 100kHz. In practice it is difficult for passive gyros to reach a finesse of 100, whereas active ring laser resonator gyroscopes can have finesse as high as 10,000.

The optical and electrical layout for an RFOG is shown in Figure 9. The light from the laser passes through an isolator and a polarizer before being split at the first 3dB coupler. The isolator protects the laser from coherent backscatter and the polarizer ensures that the light launched into the resonator is linearly polarized. After the 3dB coupler both the CW and CCW light paths pass through a phase modulator. The phase modulator applies the serrrodyne modulation and the bias modulation to the light paths. Each path then passes through a circulator and to the resonator coupler. The resonator coupler allows only 1 to 2% of the light to enter the resonator. The circulator diverts the light exiting the resonator to the photodetector. A phase sensitive detector, PSD, at the bias frequency, demodulates the response measured by the photodetector and the signal is used as the feedback (through a voltage controlled oscillator, VCO) for the serrrodyne modulation servo loop. In this way both the CW and the CCW paths are maintained at resonance. The gyro rate is then determined by measuring the difference in serrrodyne modulation frequencies applied to the different paths.

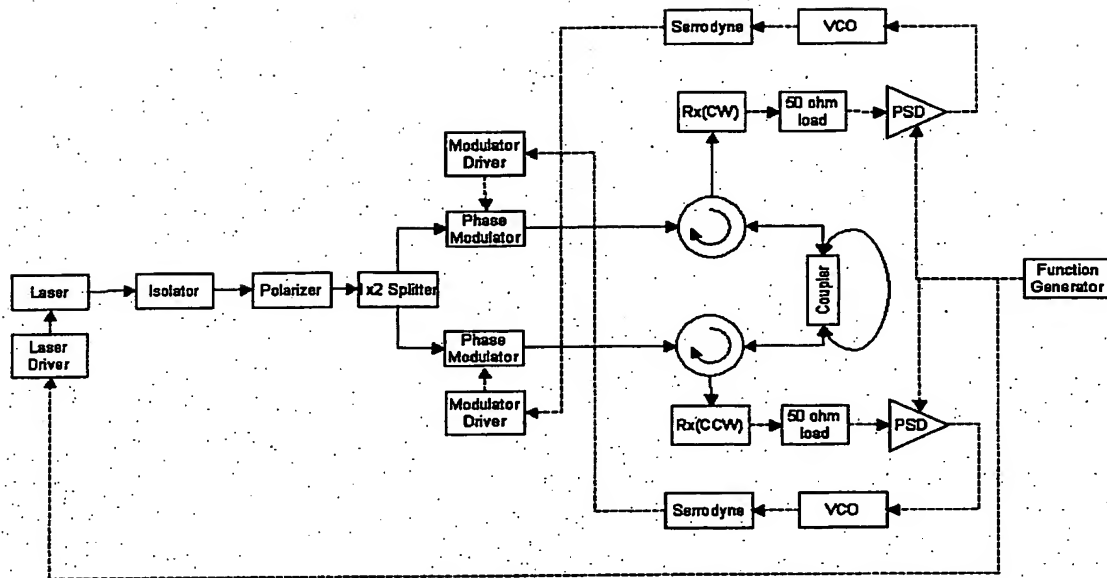


Figure 9 Electrical and optical layout of an RFOG

The minimum detectable rate of the RFOG can be calculated by analyzing the shot-noise limit of the detector. The photodetector used to measure the power output of the resonator has a minimum detectable power level due to noise^{13, 14}. The noise equivalent power, NEP , of a photodetector is defined as the input power required to just be able to measure a signal (point at which the signal to noise ratio is equal to 1). Mathematically this is equivalent to

$$P_{NEP} = \frac{i_{rms}}{R} \quad (13)$$

where R is the responsivity of the detector, in A/W , and i_{rms} is the root-mean-square current out of the photodetector over a specified frequency range.

As one samples the photodetector output for a longer period of time, it becomes easier to measure a signal since the random noise may be averaged away. Because of this, manufacturers typically specify the noise equivalent power spectral density ($NEPSD$) of a detector using

$$P_{NEP} = P_{NEPSD} \sqrt{B} \quad (14)$$

¹³ A. Bruce Buckman. *Guided-Wave Photonics*. Saunders College Publishing, Orlando, FL, 1992.

¹⁴ S. Ezekiel and S.R. Balsamo. Passive ring resonator laser gyroscope. *Applied Physics Letters*, 30(9):478-480, May 1977.

where P_{NEPSD} is the $NEPSD$ and B is the bandwidth of the detector. As the bandwidth of the detector decreases sampling times become longer and the P_{NEP} decreases so that a smaller signal may be measured.

In the RFOG we will assume the minimum power that can be measured by the photodetector is given by (14) where the photodetector bandwidth will be set by the RFOG feedback system. Assume that the laser has an output power of P_{laser} , where there are L_{in} (dB) losses between the laser and resonator, and L_{out} (dB) losses between the resonator and detector. The power at the detector may then be defined by

$$P_{detector} = 10^{-(L_{out}+L_{in})/10} \frac{E_0^* E_0}{E_i^* E_i} P_{laser} \quad (15)$$

where we have used the resonator power response defined by (11). Using (15) it is possible to determine the minimum phase change δ_{min} which yields a detector power change greater than P_{NEP} .

Simplifying (15) yields a resonator power response

$$P_d - P_{NEP} = \frac{P_d}{1 + b^2 \sin^2(\delta/2)} \quad (16)$$

Where P_d is the power difference between the maximum and minimum detector power and

$$b = \frac{1}{\sin(\pi/F)} \quad (17)$$

We will now find the minimum phase change δ_{min} such that the detector power changes by P_{NEP}

$$P_d - P_{NEP} = \frac{P_d}{1 + b^2 \sin^2(\delta_{min}/2)} \quad (18)$$

Solving for δ_{min} we find

$$\delta_{min} = 2a \sin\left(\frac{1}{b} \sqrt{\frac{P_d}{P_d - P_{NEP}}} - 1\right) \quad (19)$$

Once the minimum measurable phase change is determined, the minimum measurable frequency shift may be obtained using

$$f_{min} = f_{fsr} \frac{\delta_{min}}{2\pi} \quad (20)$$

where f_{fsr} is the free spectral range defined by

$$f_{fsr} = \frac{c}{nL} \quad (21)$$

where n is the refractive index, and L is the fiber coil length. Given that

$$K = \frac{|f_1 - f_2|}{|\Omega|} \approx \frac{4NA}{nL\lambda}, \quad (22)$$

where K is the gyroscope gain, we can conclude that the minimum detectable angular rate is given by

$$\Omega_{min} = \frac{f_{min}}{K} \quad (23)$$

where K is the gyro gain.

Note that Ω_{min} is calculated in terms of the photodetector bandwidth since it affects P_{NEP} . Thus (23) defines the minimum angular rate detectable by the control system for a single sample. For navigation, however, one is usually interested in the minimum detectable rate over a longer period (e.g. over a one second window). The minimum rate is thus redefined as

$$\Omega_{min} = \frac{f_{min}}{K} \sqrt{\frac{B_s}{B_e}} \quad (24)$$

where B_s is the sample bandwidth of interest and B_e is the bandwidth at which the electronics calculate an angular rate.

The above discussion takes only the limitation of the detector electronics into account for determining the minimum resolvable rotation rate of a gyroscope. Because the counterpropagating light waves are traveling through a dielectric medium, phase shift unrelated to the Sagnac effect can occur.

2.1.2. Kerr Effects

The Kerr effect is a third order non-linear effect that describes intensity dependent perturbations of the propagation constant of the fiber^{15,16}. The perturbations of the propagation constants are:

¹⁵ R.A. Bergh, H.C. Lefevre and H.J. Shaw. Compensation of the optical Kerr effect in fiber-optic gyroscopes. *Optics Letters*, 7(6):282-284, June 1982.

¹⁶ K. Iwatsuki, K. Hotate and M. Higashiguchi. Kerr Effect in an Optical Passive Ring-Resonator Gyro. *Journal of Lightwave Technology*, LT-4(6):645-651, June 1986.

$$\begin{aligned}\beta_{k1}(z,t) &= \frac{4\pi\eta n_2}{\lambda} \delta[I_1(z,t) + 2I_2(z,t)] \\ \beta_{k2}(z,t) &= \frac{4\pi\eta n_2}{\lambda} \delta[I_2(z,t) + 2I_1(z,t)]\end{aligned}\quad (25)$$

where η is the impedance of the medium, λ is the wavelength in a vacuum, n_2 is the Kerr coefficient of the medium, and δ is a factor of order unity that depends on the transverse distribution of the mode. $I_1(z,t)$ and $I_2(z,t)$ are the wave transverse peak intensities. It is the factor of 2 between the wave intensities that gives rise to non-reciprocity if the wave intensities are not the same.

The Kerr phase, $\phi_k = \Delta\beta L$, can be used to estimate the Kerr-induced bias:

$$\Omega_k = \frac{\lambda c}{4\pi R L} \phi_k \quad (26)$$

Studies have shown that the drift due to the Kerr effect can become larger than the theoretical limit of rotation sensing given by the detector shot noise. The Kerr induced bias can be eliminated by using a low-coherence (wide bandwidth) source where the optical field amplitude has a Gaussian probability distribution and statistically gives no net phase. However, a coherent (narrow bandwidth) source is required for the RMOG to maintain a high finesse. For RMOG's the Kerr effect can determine the minimum measureable rate. One method utilized to compensate for the Kerr effect in RMOG's is to modulate the source intensity to adjust the nonlinear interaction between the counterpropagating waves.

2.1.3. Stress Birefringence

Theoretically, a single mode optical fiber should maintain linear polarization states over long lengths. However, optical birefringence due to stress results from fiber bends, twists and non-ideal core geometry. This stress birefringence can result in gyro drift. The effects of birefringence can be eliminated by polarizing the light source and utilizing polarization maintaining fiber. In this way the polarized light experiences a single effective index. However, care must be taken to not induce polarization mode hopping.

2.1.4. Rayleigh Scattering

Rayleigh scattering in a fiber is caused by the dipole moment induced by the refractive index fluctuation, $\Delta n(x,y,z)$, in the fiber under the incident electric field¹⁷. Part of the scattered field is reflected back in the single mode fiber as the fundamental mode. Because the backscattered light is coherent with the primary light they can interfere and cause a rotation rate error. With an IFOG the use of an incoherent source reduces the amount of coherent scattering. However, an RMOG requires the use of a coherent source. The Rayleigh scattering induced noise in RMOG has been eliminated by phase or frequency modulation of both launching paths driven at different frequencies.

¹⁷ K. Iwatsuki, K. Hotate and M. Higashiguchi. Effect of Rayleigh backscattering in an optical passive ring-resonator gyro. *Applied Optics*, 23(21):3916-3924, November 1984.

2.2. Signal Processing

A highly important facet of any optical gyro development is the gyro's signal processing. The next two sections discuss the foundations of the signal processing that has evolved for fiber optic gyroscopes and has contributed heavily to the success of present day devices.

2.2.1. Biasing

The rotation induced phase shift of Sagnac interferometers is linearly proportional to the rotation rate. However, the light intensity response of an optical gyroscope is proportional to a raised cosine function, therefore, it is non-linear and periodic. This response is characterized by zero sensitivity at $n\pi$ (n :integer) phase shift including zero phase shift. Also, the symmetry of the response curve at phase shift of $n\pi$ makes the direction of rotation ambiguous. Finally, at high speed of rotation the periodicity of the response makes phase determination impossible. The periodicity is solved by initiating the gyroscope at a zero rotation rate. The remaining issues can be addressed by dynamically biasing the gyroscope.

The idea of dynamic biasing is to offset the gyro response curve by $\pi/2$ resulting in a maximum sensitivity at $n\pi$ phase shift (including zero phase shift) and an unambiguous relationship between phase shift and intensity. Dynamic biasing is accomplished by switching the gyroscope operating point between $+\pi/2$ and $-\pi/2$ of differential phase shift with 50% duty cycle. Using a sinusoidal phase modulation $\Delta\phi(t) = \phi_m \sin(\omega_m t)$ the detector current, $I_d(t)$, is

$$I_d(t) = I_0 / 2 \left[1 + \cos(\phi_m \sin \omega_m t + \phi_R) \right] \\ = I_0 / 2 \left[1 + \left\{ J_0(\phi_m) + 2 \sum_n J_{2n}(\phi_m) \cos(2n\omega_m t) \right\} \cos(\phi_R) - 2 \sum_n J_{2n-1}(\phi_m) \sin\{(2n-1)\omega_m t\} \sin(\phi_R) \right] \quad (27)$$

where I_0 is the peak detector intensity and J_n is the n th order Bessel function of the first kind. By adjusting the amplitude of the phase modulation frequency to 1.84 radians, where $J_1(\phi_m)$ is a maximum, and measuring the amplitude of the detector current at the first harmonic of the phase modulation frequency, $I(\omega_m)$, using a lock-in amplifier the gyroscope response is sinusoidal.

2.2.2. Closed Loop Operation

For closed loop operation of a gyroscope a nonreciprocal phase shift is introduced between the counterpropagating optical waves to compensate for the rotation induced Sagnac phase shift. The phase difference between the counterpropagating waves is kept at zero by a feedback servo loop using the detector output as the error signal. The amount of nonreciprocal phase shift introduced is the measured output of the gyroscope and is a linear function of rotation rate. One method commonly used to achieve the nonreciprocal phase shift is analog serrodyne modulation using phase modulators. Phase modulators are inherently reciprocal devices, therefore, they are placed at asymmetric positions on the sensing loop so that the counterpropagating waves pass through them at different times before they interfere with each other. To produce a time

varying phase difference between the counterpropagating waves with a time averaged phase shift of zero, the phase modulator must produce a linear phase ramp with respect to time. It is impossible for a phase shifter to create an infinitely increasing phase modulation with time; therefore, serrodyne modulation is used.

Serrodyne modulation uses a sawtooth waveform with a modulation amplitude of 2π . By choosing a 2π modulation amplitude the effects of the flyback on the gyro are eliminated due to the 2π periodicity of the gyroscope response. The amount of differential phase shift applied is controlled by the frequency of the sawtooth waveform. Either analog or digital sawtooth waveforms have been used to produce the non-reciprocal phase shift.

3. Gyro Breadboard

3.1. Purpose

A breadboard passive resonant fiber optic gyroscope was fabricated from COTs parts. The purpose of the breadboard was to verify our computational models, evaluate electronic control designs and generally gain hands-on experience with fiber optic gyroscopes.

3.2. Breadboard Design

The theoretical minimum measurable rotational rates were calculated using the formalisms outlined in section 2.1.1. Vendor information from COTs components was used for the analysis. In this analysis we assumed the following when choosing the components:

1. The resonator coupling coefficient should be chosen to obtain the lowest measurable angular rate for a given coil geometry.
2. The modulation range should be at least 1.5 times the free spectral range for the feedback electronics. This assumes no frequency shifts due to platform angular rate.
3. The laser linewidth should be smaller than half the resonator linewidth.

The input and output power losses for the two designs are based on a 3dB power loss at each 1×2 splitter, a 1dB loss due to the isolator/polarizer, and a 3dB loss at the phase modulators. The resonator coupler loss is the power loss that occurs during each pass through the coupler in addition to the loss due to the split of the signal. For example, if a 1×2 coupler has an overall power decrease of 4.2dB, then there is a 1.2dB coupler loss since a 3dB power attenuation (i.e., 50%) is the decrease in a perfect coupler. We will assume that the minimum measurable rate will be based on a 1 second average so $B_s = 1$. We will also assume that $B_e = 40000$ so that

$$\sqrt{\frac{B_s}{B_e}} = \sqrt{1/40000} \quad (28)$$

In the analysis to follow we will study the theoretical performance of a resonator with both 10 loops and 30 loops. As a comparison, a Litton LN200 (based on an IFOG design)

has a minimum measurable rate of 1deg/hr and a X-Bow unit has a minimum measurable rate of 3600deg/hr.

For both designs the following parameters were used:

Laser Power (mW)	20
Laser Wavelength (nm)	1550
Phase Modulation (MHz)	40
Resonator Input Loss (dB)	10
Resonator Output Loss (dB)	3.5
Resonator Coupler Loss (dB)	0.75
Resonator Fiber Loss (dB/m)	0.01
Fiber Refractive Index	1.5
Diameter of Resonator (cm)	10
Detector NEPSD (pW/ $\sqrt{\text{Hz}}$)	3
Detector Bandwidth (kHz)	40

Figure 10 shows the calculated minimum detectable rate as a function of fiber length for a 10cm diameter resonator. The ideal coupling was calculated to be 0.955. For 10 loops (3.14 meters) the minimum detectable rate is 35deg/hr. For 30 loops (9.42 meters) the minimum rate is 14 deg/hr. The finesse of the 10 loop and 30 loop resonators are 32 and 27, respectively. The linewidths of the 10 loop and 30 loop resonators are 2MHz and 0.7MHz, respectively. The free spectral range of the 10 loop and 30 loop resonators are 63MHz and 21MHz, respectively.

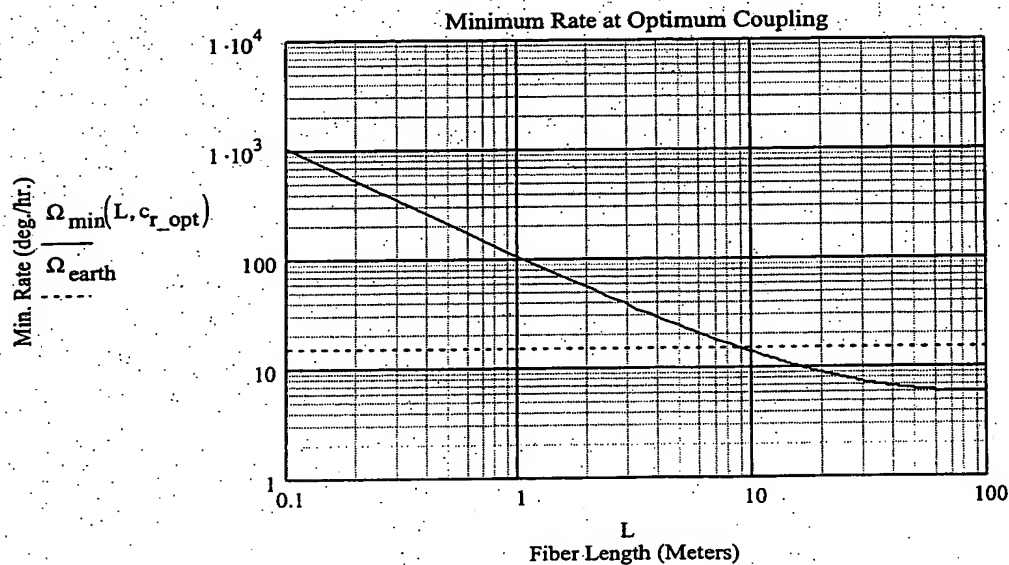


Figure 10 The red line is the minimum detectable rate at ideal resonator coupling for a 10cm diameter resonator. The dotted blue line is earth rate (15 deg/hr).

3.3. Breadboard Components and Configuration

A schematic of the breadboard gyroscope is shown in Figure 11. Based on the results of the RFOG simulation, COT's parts were purchased and a breadboard 10cm diameter 10 turn RMOG was fabricated. Table 2 lists the optical components used for the RMOG breadboard.

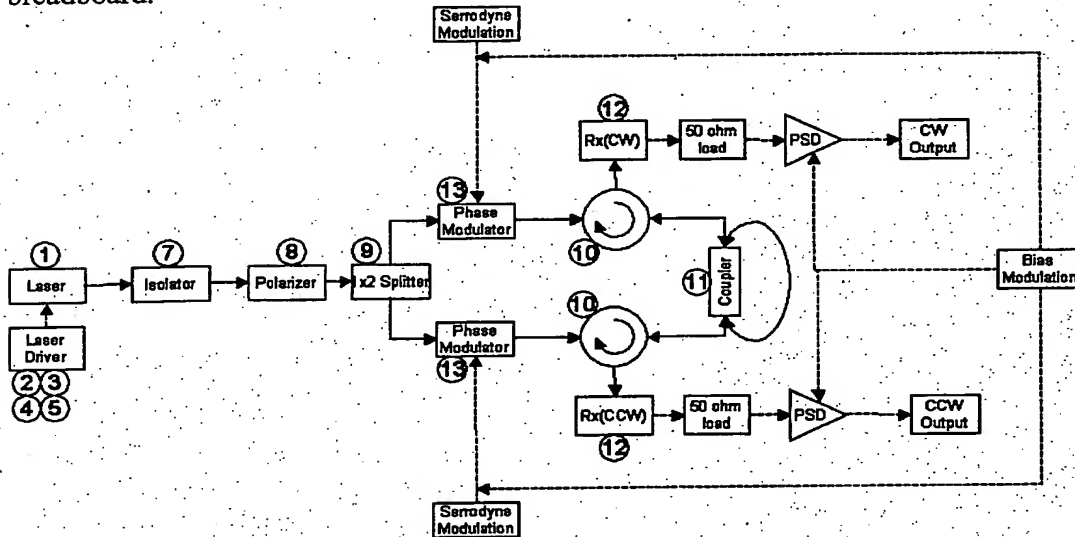


Figure 11 Electrical and optical schematic of the breadboard gyroscope system. The numbers correspond to the numbers in Table 2

To minimize coupler losses and backreflections due to fiber splice, specialty resonators were fabricated where the resonator is a continuous loop of fiber. The resonators were fabricated by Canadian Instrumentation and Research and are model 905P variable couplers with single mode polarization maintaining fiber. Polarization maintaining 3dB couplers and circulators were purchased from Oz optics. The 1550nm laser is model CQF938/40 from JDS Uniphase. The laser is controlled by a Newport model 910P laser and a model 325 temperature controller. Phase modulators were purchased from EOSpace, fabricated with polarization maintaining fiber and have a V_{π} of 7.2V. A Tektronix 610P arbitrary waveform generator generates the analog serrodyne waveform. A wide bandwidth RF amplifier amplifies the signal from the AWG. The bias modulation was provided by a Pragmatic 2414A 20MHz arbitrary waveform generator. A Palo Alto Research model 200 lock-in amplifier was used to demodulate the gyroscope signal.

Table 2 COTs optical and electrical components used to fabricate the RMOG breadboard

Number	Company	Model Number	Description
1	JDS Uniphase	CQF938/40	High Power DFB laser, 1550nm, polarization maintaining fiber
2	Newport Corp.	744	Butterfly telecom laser diode mount
3	Newport Corp.	505	Laser diode drive 200/500 mA
4	Newport Corp.	500-02	Laser Diode Driver Cable
5	Newport Corp.	325	Laser Diode Temperature Controller, 15 watt
6	Newport Corp.	300-02	Temperature Controller Cable
7	Oz Optics	FOI111115509/125P603A,3A30.560	Fiber optic pigtailed isolator, 1550nm, 0.5m PM fiber, 60 dB back reflection, angled FC connectors on input and output
8	Oz Optics	FOP111115509/125PP603A,3A30.5ER=30	Fiber optic pigtailed polarizer, 1550nm, 0.5m PM fiber, 60 dB back reflection, angled FC connectors on input and output
9	Oz Optics	FOBS12P1119/125PP P155050/50603A,3A,3A30.5ER=30	Fiber optic pigtailed 1x2 beam splitter, 1550nm, 0.5m PM fiber, 60 db back reflection, angled FC connectors on input and output
10	Oz Optics	FOC12P1119/125PPP1550603A,3A,3A30.5ER=30	Fiber optic pigtailed circulator, 1550nm, 0.5m PM fiber, 60 dB back reflection, angled FC connectors on input and output
11	Canadian Instrumentation & Research	905P variable coupler	Model 905P variable coupler with 3.2 meter loop, including 10 turns on 10cm diameter form. Polarization maintaining fiber of approximately 9/125 (core/cladding) diameter. 1 meter long fiber pigtails on input and output. Bare fiber ends, no connectors.
12	Thor Labs	DET410	Photo detector
13	EOspace	PM-0K0-12-PFA-PFA-S	Lithium niobate phase modulator without terminating resistor, Insertion Loss < 3 dB, 3 db Bandwidth > 12.5 GHz, Modulation Port $V\pi$ (@ 1 GHz) < 6 volts

3.4. Experimentation Using the Breadboard

The first task was to set the resonant ring to the optimum coupling coefficient. To set the coupling coefficient the laser frequency was swept across the resonant frequency of the RMOG by modulating the drive current with a 20mA_{pp} sine wave. Modulating the drive current results in a modulation of the laser wavelength as characterized in Figure 12. The

output of the resonator was monitored by a photodetector that was read by an oscilloscope. At the optimum coupling coefficient no light will leave the resonator and a minimum in

intensity should be found. The caliper on the resonator was adjusted to minimize the photodetector output.

With the optimum coupling coefficient set the free spectral range and linewidth of the resonator was experimentally determined and compared with calculations. A 20mA triangle wave was used to modulate the laser drive current. The current modulation waveform and the associated resonator

output are shown in Figure 13. The laser is swept across ~5 resonances of the RMOG resulting in several minima. The smaller dips in detector intensity between the larger resonances are resonances due to a small amount of polarization crossover in the system. The frequency differences between several resonances were averaged and the free spectral range was found to be ~60MHz, consistent with the calculated free spectral range of 62MHz. The resonator linewidth was determined to be ~2MHz, consistent with the calculated value. Given the small linewidth of the resonator the laser could not be tuned to resonance using current tuning. Serrodyne modulation was used to adjust the frequency to resonance.

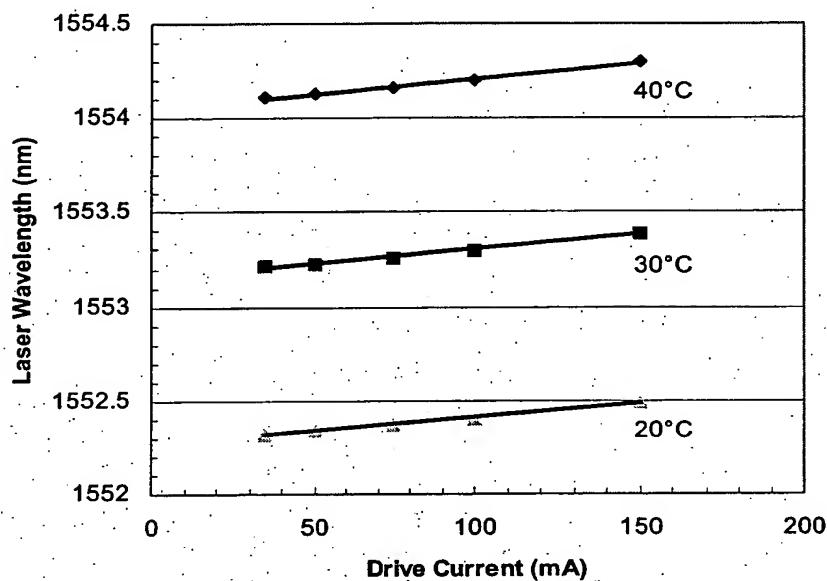


Figure 12 The dependence of laser wavelength on temperature and drive current.

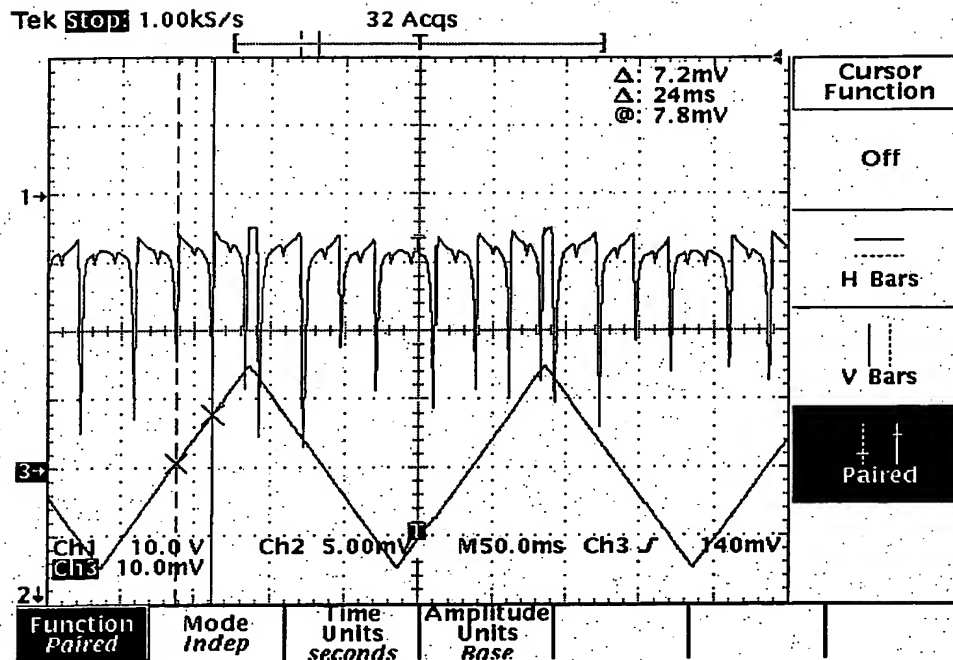


Figure 13 RFOG resonances as a function of laser current

An arbitrary waveform generator was used to generate a 60MHz sawtooth waveform with $<2\text{ns}$ flyback, see Figure 14. Only 3.5V_{pp} could be obtained from the AWG; therefore, as shown in, the signal was amplified to 14.4V_{pp} by a 1GHz RF amplifier. 14.4V_{pp} is necessary to achieve a 2π phase shift on the phase modulators. A shift of 2π eliminates the effects of the flyback due to the 2π periodicity of the gyroscope response. The change in frequency shift is controlled by the frequency of the serrodyne waveform. Only the linear portions of the phase ramp will produce a stable frequency shift; therefore, the fidelity of the waveform is paramount. As shown in Figure 15, the quality of the 60Mhz waveform directly out of the AWG is compromised. When amplified the waveform is further degraded. The result is that a stable frequency shift could not be achieved. Without the ability to shift the frequency to resonance, gyroscope data could not be obtained.

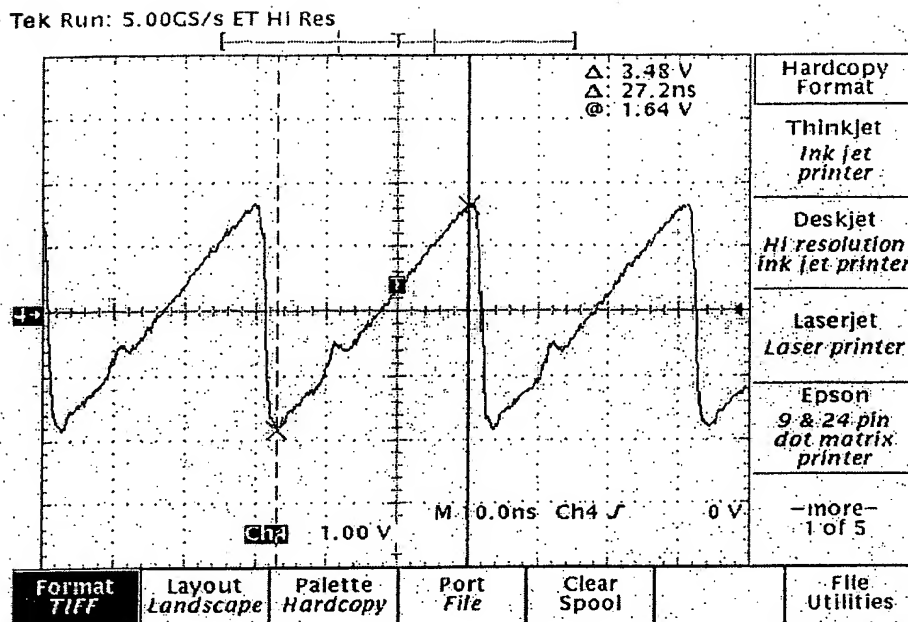


Figure 14 The analog serrordyne waveform produced by the arbitrary waveform generator

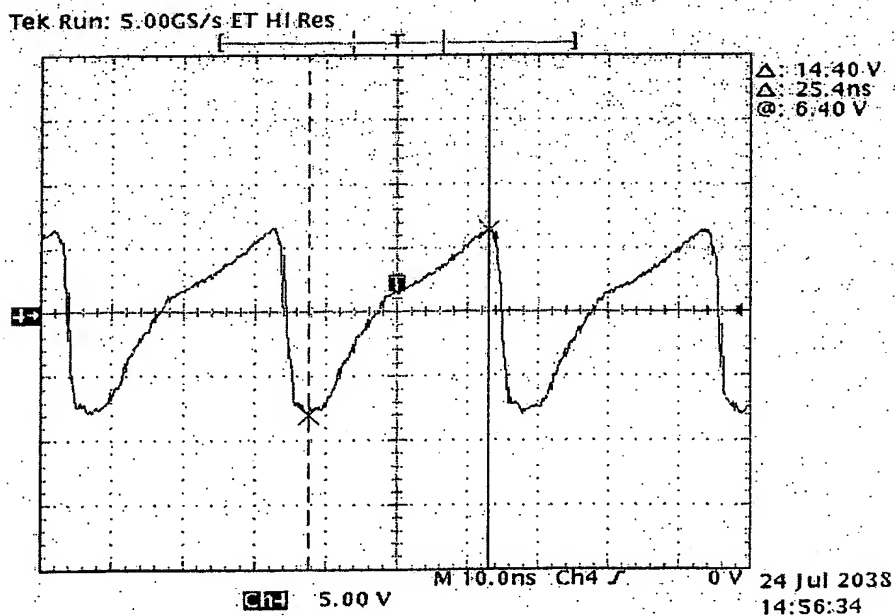


Figure 15 The analog serrordyne waveform after amplified to a V_{pp} of 14.4V necessary to reach a 2π phase shift on the phase modulators

3.5. Future Work

The difficulties encountered with analog serrodyne modulation can be overcome by using digital serrodyne modulation. Digital serrodyne modulation has been used extensively for fiber optic gyroscopes¹⁸. Instead of a ramp, the modulator provides steps of phase with duration t_d , the transit time in the coil. These are reset synchronously with the bias modulation so that the flyback noise can be gated out. The output is a count of the number of phase steps between resets. This approach not only solves the issues with frequency noise due to voltage ripple in the analog approach, but can also be implemented using digital signal processors.

4. Hybrid Photonic Approach

The focus of this development effort was on an RFOG as described in the previous sections. Our ultimate goal is to create an integrated version of the RFOG where all of the components are integrated onto a single rigid platform termed the resonant micro-optic gyro (RMOG). This vision includes replacing the loose fiber loop with a spiral waveguide formed on a rigid semiconductor, coupled to a sub-chip assembly containing the laser, modulator, and detector components. This section discusses the contributing advances towards the realization of this system achieved during the LDRD term. The objective of this work involved developing the technical foundation required to fabricate the individual RMOG components.

The two sub-chip assemblies of the RMOG include the optical waveguide resonator ring, and the active semiconductor. The PIC contains the optically active laser and detector, the optically passive phase modulators and the active-passive low-loss waveguiding interconnects. Refer to Figure 16. In an effort to maximize the system sensitivity and minimize loss, the integrated resonator loop is to be formed in high-performance silica material. The spiral resonator waveguides form a silica planar lightwave circuit (PLC) on a silicon wafer and were fabricated in the MESA East CMOS facility using technology recently developed for low-loss telecom switches. Development of the PLC portion of the RMOG was not a funded component of this LDRD program as this technology is significantly more mature than semiconductor photonic integrated circuits (PICs). The development of the sub-chip components that required optically active semiconductors occurred in the MESA West compound semiconductor facility using AlGaAs material. In our vision, the elements formed in active material (the laser, modulator, and photodiodes) will be monolithically integrated into a compact semiconductor PIC on a small GaAs substrate. The silica PLC and semiconductor PIC will then be joined along one edge to form a complete solid-state integrated optical system. Refer to Figure 16 and Figure 17. The resulting micro-optic gyro would be small and rugged, as well as inexpensive. Fabrication is simplified and low-cost realizable as each of the two sub-chips employs a technology optimized for its function. In volume production, a dozen or more of the PIC and PLC chips could be fabricated on a single substrate. The chip-to-chip alignment and joining is readily achieved using commercially available tools. Generally this involves alignment of the waveguides, attachment of the two chips using

¹⁸ Anthony Lawrence. *Modern Inertial Technology*. Springer, New York, Second Edition, 1998.

optical adhesive, and firmly mounting the assembly onto a rugged thermally and electrically conductive substrate such as copper.

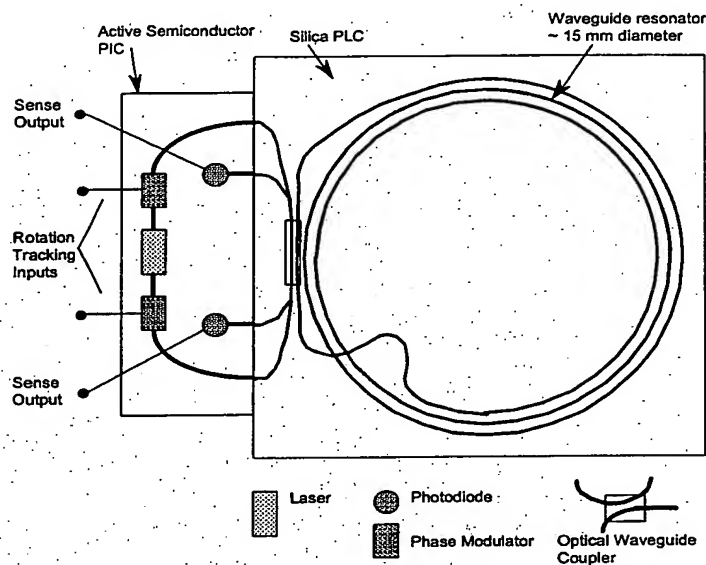


Figure 16 Schematic of resonant micro-optic gyro, RMOG

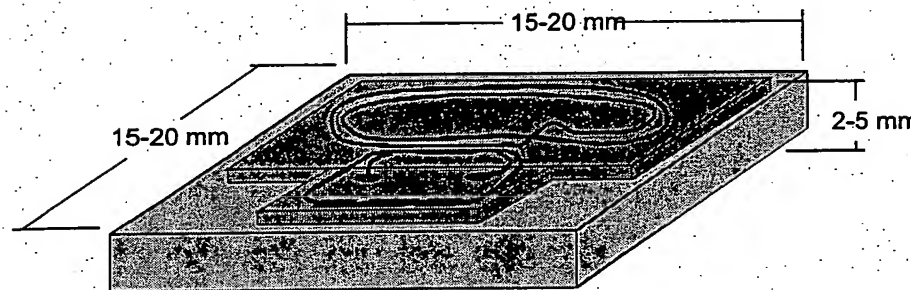


Figure 17 View of resonant micro-optic gyro, RMOG, hybrid Photonic chip showing relative locations of the PIC (blue) and PLC (gray) on the common rugged mount and heatsink (yellow)

4.1. Development of the Semiconductor PIC Components

A portion of the final year of this program was dedicated to exploring issues and options regarding the feasibility of integrating a gyro into a single monolithic photonic circuit. For this task, effort was divided into two technically central issues of the RMOG active PIC sub-chip: (1) develop the technology in the form of fabrication processes to realize the narrow-linewidth laser and (2) develop the base active-passive interconnect

technology. The laser itself is a key element limiting gyro performance via the spectral linewidth. The project explored means to build narrow-linewidth (less than 2-3 MHz) lasers in a monolithically integrated format. Active-passive integration is a key technology that provides low-loss interconnecting waveguides. Active/passive integration will be achieved by means of selective-area quantum-well disordering. The disordering technology enables optically passive devices (such as phase modulators, and interconnecting waveguides) to be fabricated in epitaxial semiconductor material that was designed for active components (such as lasers and photodetectors). For example, the modulators and passive interconnects will be formed in the passive-disordered material and the laser and photodiode will be formed in the active-nondisordered material. The goal of this work was the development of a broadly capable basis set of devices and optical integrated circuit technology suited for a wide variety of optical gyro designs or for other wavelength-dependent sense and control applications. For example, the AlGaAs PIC could be readily used to work with resonator loops made from other materials such as optical fiber or photonic crystals.

4.2. Design Criteria

The focus of this effort primarily involved developing the technology required to fabricate the individual RMOG components. However, the processes developed were generic enough to provide flexibility in design and fabrication space to include optimum performance designs in successive work. The component specifications of the semiconductor PIC portion of the RMOG include: the fabrication of a coherent laser source, a bidirectional distributed feedback (DFB) laser with a spectral linewidth of less than 500 kHz, greater than 15 mW output power from each end, an optical phase modulator with a voltage-phase figure-of-merit of $25 \text{ degrees} \cdot \text{volt}^{-1} \cdot \text{mm}^{-1}$, a waveguide photodiode with 90 percent efficiency, and non-absorbing interconnecting optical waveguides with less than 1 dB/cm loss for routing light between the above devices and to the PLC loop waveguide. Figure 18 presents a cross-section view of these components in an integrated format.

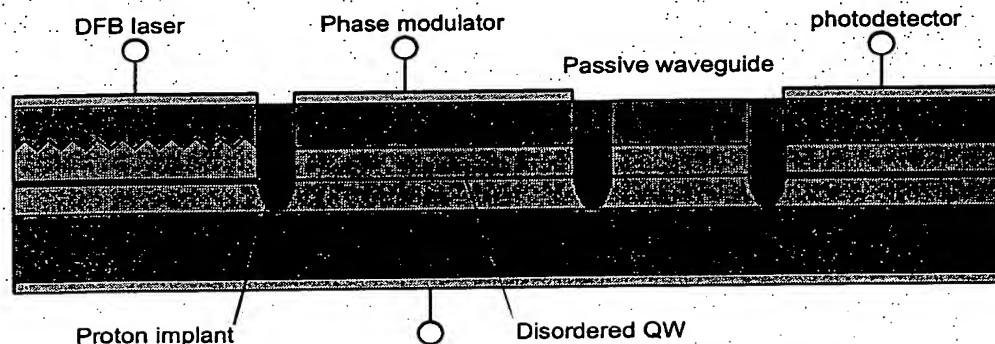


Figure 18 Schematic diagram of the active sub-chip assembly

In addition to the components' optical specifications, electrical isolation requirements of the PIC assembly were addressed. Since phase modulators and photodiodes will be

reverse biased, electrical isolation between the forward-biased laser and other areas of the PIC will be achieved by means of the well-known method of proton or oxygen ion implantation.¹⁹ It is also possible that forward-biased phase modulators will prove useful. Under forward bias current injection, very strong phase (refractive index) modulation is possible although this effect is also accompanied by absorption effects that may preclude this mode of operation. Electrical isolation by implantation will enable the flexibility to explore these bias options.

4.3. Progress towards Component Realization

4.3.1. AlGaAs DFB laser for photonic integrated circuits

One critical component necessary for high-performance gyro operation is the laser source. Two aspects are of importance: (1) the output power and efficiency laser characteristics and (2) a narrow linewidth goal of ~ 500 kHz required for proper resonator loop functionality.

The epitaxial structure chosen for the RMOG is of the buried oxide waveguide (BOW) type. Refer to Figure 19.

This structure consists of a single GaAs quantum well surrounded by AlGaAs barriers. Thin layers of AlAs are included in the cladding. The lateral waveguide is formed by exposing the AlAs layers to a deep mesa etch and selectively oxidizing to push the optical mode away from the etched sidewalls. This approach creates highly efficient, low-threshold-current edge-emitting lasers where both the optical waveguide and lateral current confinement are achieved by lateral selective oxidation of AlGaAs.²⁰ Using these concepts, external differential quantum efficiency in excess

of 95% and 40% wall-plug efficiency have been demonstrated. We have also recently explored use of selectively oxidized waveguides for low-drive-voltage high-speed optical phase modulators and electroabsorption modulators suitable for >40 Gb/s optical

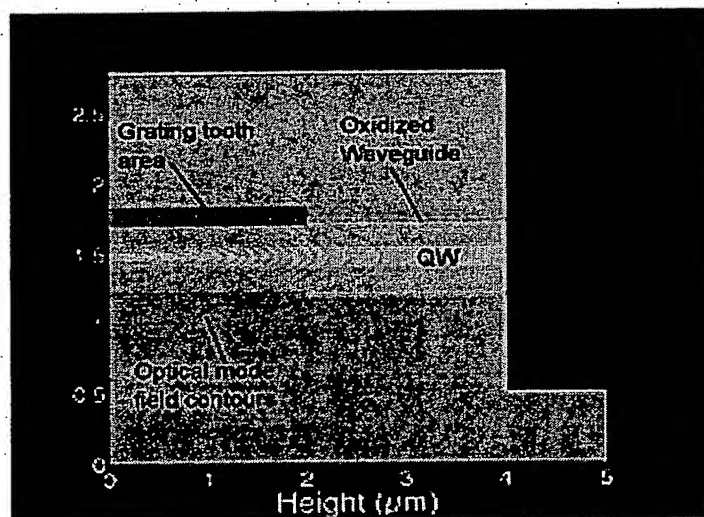


Figure 19 Cross-section of BOW structure showing the electric field contours overlapping the grating tooth area. The optical mode is distributed about the quantum well (QW) and contained by the oxidized waveguide.

¹⁹ G. A. Vawter, A. Mar, V. Hietala, J. Zolper, and J. Hohimer. "All optical millimeter-wave electrical signal generation using an integrated mode-locked semiconductor ring laser and photodiode" IEEE PTL, Vol 9, No 12, Dec. 1997, pg 1634.

²⁰ G. A. Vawter, O. Blum, A. Allerman, Y. Gao. "Highly-efficient laser with self aligned waveguide and current confinement by selective oxidation" IEEE LEOS Conference Proceedings, 1999, Vol. 2, pg 531.

modulation. This high-performance is a result of placement of the oxide layers so as to achieve the minimum optical mode size. The small mode size increases the confinement factor of the laser and reduces the required applied electric field excursions of modulators.

The second critical aspect is the choice of an integrated laser geometry that would satisfy the high-Q laser cavity performance. The laser design criteria required development of a new type of distributed-feedback laser (DFB). This new laser uses selective dry etching of gratings in AlGaAs with an InGaP chemical stop layer coupled with AlGaAs epitaxial regrowth to form the low-index-contrast grating needed by high-quality narrow-optical-spectrum lasers. See Figure 19. A central part of this effort has been the development of epitaxial regrowth on InGaP surfaces over thick AlGaAs layers as shown in Figure 20. This technology enables use of a regrown grating permitting current injection through the grating region for either uniform gain or for wavelength tuning to assist in locating the gyro resonance.

4.3.2. Active/passive integration technology based on selective-area disordering

The integration of active and passive devices is accomplished through an impurity free vacancy diffusion (IFVD) quantum well intermixing process.²¹ The regions that will remain active are covered with SiN_x while the regions that are to be passive are covered with SiO₂. The sample is annealed in a rapid thermal anneal (RTA) system at 900° C for 4 minutes. During this time, Ga diffuses into the SiO₂ leaving behind group III vacancies in the GaAs cap.

Intermixing (disordering) occurs in the GaAs quantum well as the vacancies intermix the group III atoms in the quantum well and its barriers. The result is the change from a square-well potential to a rounded or parabolic shaped potential. The bandgap energy is increased, moving this disordered regions gain curve, photoluminescence (PL) spectrum, and absorption edge to shorter wavelengths (up to 70 nm). The bandgap of the non-disordered region remains as designed with a small change in PL peak (1-10 nm) caused by the intrinsic vacancies of the material that intermix within the quantum well. The resulting selectively intermixed PIC contains non-disordered active regions with corresponding gain, PL, and large absorption characteristics at a wavelength tailored by the quantum well structure, and

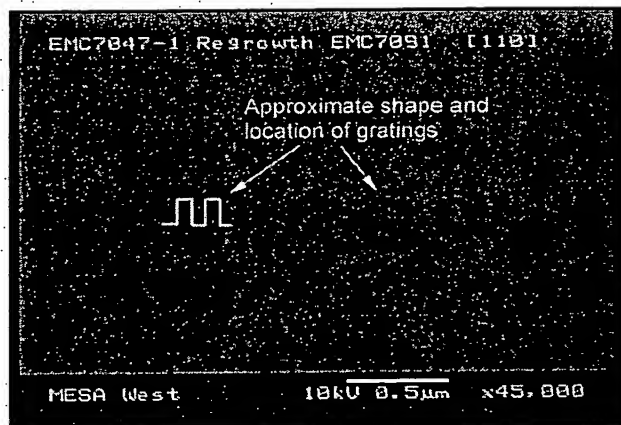


Figure 20 Electron microscope cross-section image of regrown gratings. The outline highlighted in white shows the approximate grating profile. Low contrast and low discrimination between the lower grating region and upper regrown region is expected in a successful homogeneous regrowth.

²¹ D. Hofstetter, B. Maisenholder, and H. P. Zappe, "Quantum-well intermixing for fabrication of lasers and photonic integrated circuits," IEEE J. Select. Topics in Quantum Electron. 4, 794-802 (1998).

disordered, passive sections with its gain and loss characteristics blue shifted to the extent that they are low-loss passive interconnects at the lasing wavelength.

Previously, low-loss waveguides through quantum well disordering was verified at the Mesa West facility. The objective of the work reported here was to integrate the disordering process into a standard laser fabrication process, then identify and solve problems that arose due to the addition of the disordering steps. The experiments were designed in a manner that simplifies analysis of the disordering. In summary, the fabrication issues have been identified and investigated resulting in a sequence that enables successful realization of devices. However, several fabrication related issues exist that require attention in future work.

The work related to the RMOG DFB laser employs BOW epi-material with oxidized waveguides, direct write e-beam gratings, and an epi-regrowth step to complete the device. An efficient active-passive integration development activity does require an integrated laser light source, but does not require a laser of such complexity as the BOW DFB. We were interested in understanding and optimizing the fabrication complexities that arise from the disordering implementation and simplified characterization of the devices upon fabrication completion. The desired material and processing would provide devices easy and quick to fabricate and test, understanding that the disordering and complete integration process would have to be generic enough to transfer to the BOW system in the future. The decision was made to use a Broadened Waveguide (BWG) epi-structure with optical lithography for the active-passive integration development in order to focus on the disordering process and the device integration fundamentals.²²

4.3.3. Active-Passive Integration Progress

The introduction of the disordering steps into a standard active device fabrication process concluded with a successful fabrication of active lasers and detectors with interconnecting passive waveguides. Figure 21 is an image acquired from an optical microscope of the laser active/passive waveguide detector circuit. The mirrors of the integrated laser were formed by deep etched facets. The active laser cavity is covered with an ohmic contact and is visible between the two etched facet mirrors. The passive waveguide is a disordered region and optically connects the laser to the detector. The detector is an active region with an ohmic contact. Data will be collected as future work. This assembly of components will be used to

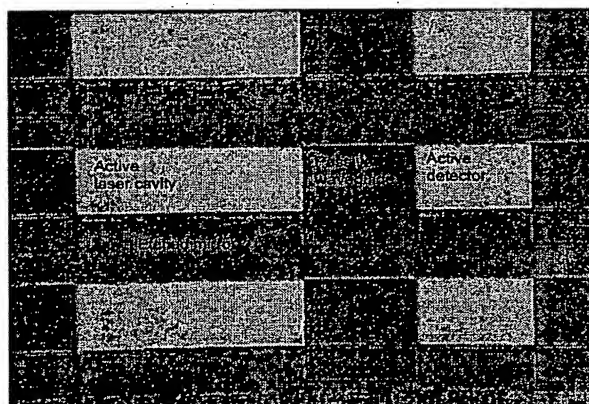


Figure 21 Image of completed active-passive integration system. Included is a laser formed by etched mirrors, passive waveguide interconnect, and a detector.

²² D. Z. Garbuzov, J. H. Abeles, N. A. Morris, P. D. Gardner, A. R. Triano, M. G. Harvey, D. B. Gilbert, and J. C. Connolly, "High power separate confinement heterostructure AlGaAs/GaAs laser diodes with broadened waveguide," in Proc. SPIE vol. 2682, 20-26.

²³ D. Hofstetter, B. Maisenholder, and H. P. Zappe, "Quantum-well intermixing for fabrication of lasers and photonic integrated circuits," IEEE J. Select. Topics in Quantum Electron. 4, 794-802 (1998).

characterize the detector performance and the coupling of light across the active and passive regions. The implementation of the disordering to the standard active device process uncovered a surface related fabrication issue. During the disorder anneal, the sample (covered with SiO₂ and SiN) is subjected to a 900° C rapid thermal anneal. Upon removal of the films, a residue is noticeable on the surface, which might prevent a low resistance ohmic contact from forming to this surface. Experiments concluded that a soak in photoresist developer (a strong base) removed the majority of residue, but a slight texturing remains as observed in the passive regions of. After ohmic contact annealing, the contacts do exhibit low ohmic resistance as desired. The developer soak is a “work-around” pertaining to this issue, however further work is required to understand why this texturing forms.

4.3.4. Experimental Evaluation of Disordered Components

Included in the fabrication were disordered passive waveguides used for evaluation of the active-passive fabrication process. Figure 22 is data from disordered waveguides showing efficient, low-loss interconnects can be formed in the disordered material.²⁴ The laser emission wavelength of this raw material was 820 nm. The disordering process blue-shifted the absorption edge approximately 50 nm. Although the data is slightly scattered, the average loss values are less than 2 dBcm⁻¹. Waveguide loss is a function of the displacement of the absorption edge from the lasing wavelength. Relevant to the disordering technology, this quantity is measured as a blue-shift of the room temperature PL peak due to disordering. Further reducing the waveguide loss would be accomplished by increasing the blue-shift.

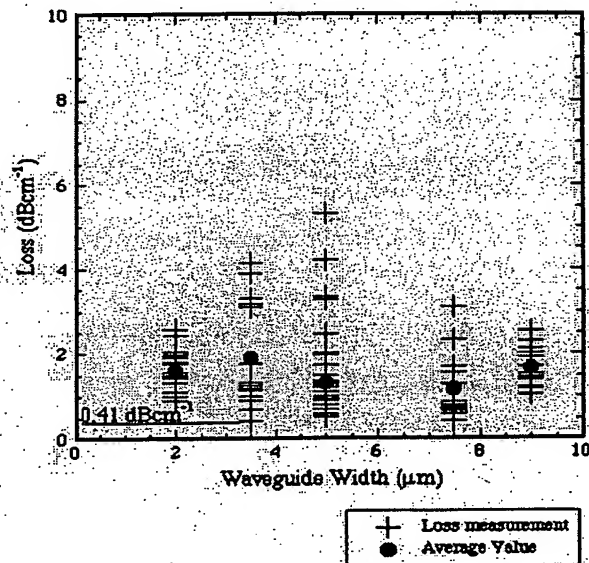


Figure 22 Waveguide loss data from material blue-shifted 50nm

²⁴ W. J. Zubrzycki, G. A. Vawter, C. T. Sullivan, A. A. Allerman, T. W. Hargett, “Low-Loss Waveguides for Active-Passive Integration using Impurity-Free Vacancy Diffusion”⁴ CLEO Tech. Digest, pg 16 (2001).

Figure 23 displays a plot of experimentally measured waveguide loss data along with the blue-shifted PL spectrum. The loss measurements were from waveguides 7 μm wide and 3600 μm long. The PL spectrum was normalized to fit the vertical scale and has no relation to that scale. The PL spectrum and the loss data points are correlated to the wavelength scale. The non-disordered (active) material had a PL peak at 830 nm as well as a lasing wavelength of 830 nm. The data presented shows less than 10 dBcm^{-1} loss at the lasing wavelength of 830 nm in material blue-shifted 42 nm. However, the data also shows that a loss of less than 1 dBcm^{-1} occurs in material blue shifted 64 nm. The BWG material repeatedly blue-shifts 30-40 nm. Further work is required to determine a means to a repeatable blue-shift increase.

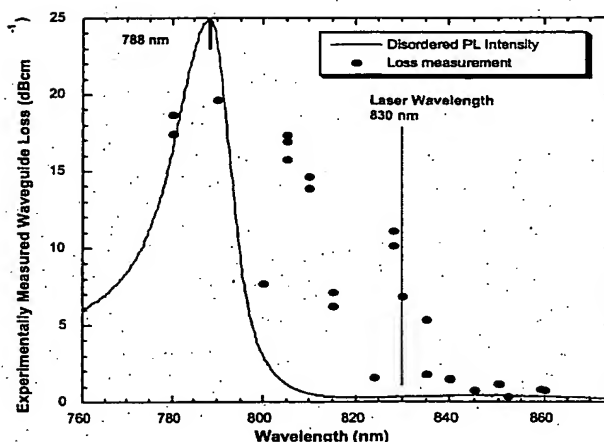


Figure 23 Loss data superimposed with blue-shifted PL spectrum and lasing wavelength. Waveguide loss as low as 0.38 dB/cm was measured at 852 nm. Knowing the wavelength distance from the blue-shifted PL peak required for 1 dB/cm loss tells us how far we have to blue-shift.

5. Summary of Accomplishments

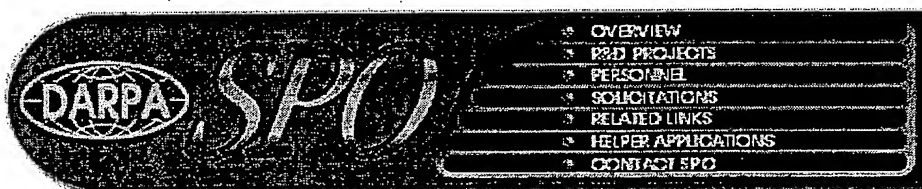
Accomplishments achieved during this development effort are as follows:

- We comprehensively surveyed the present state-of-the-art for MEMS gyros.
- We explored potential roles for gyros in nuclear weapons and achieved greater insight into the attributes required for successful incorporation of a MEMS gyro into new weapon designs or life extension initiatives.
- We developed analytical model for a RMOG thus providing a valuable tool for selecting design parameters from the available design space and focusing development activity.
- We constructed a gyro testbed from COTS parts to provide (1)an educational tool, (2)an aid to model validation, (3) a predictor of gyro performance, and (4)a provider of insight into the difficulty of implementing gyro signal processing electronics by various routes.
- We built an analog serrodyne and determined this approach to be impractical.
- We developed processes for making an integrated narrow-linewidth laser and for implementing the active/passive technology essential for integration of the laser, phase modulator, waveguides and couplers, and photodetector on a single substrate.
- We designed an AlGaAs DFB laser and a resonant ring for implementation in silicon replacing the less robust optical fiber ring initially proposed.

- **We built test structures for validating and characterizing active/passive integration processes.**

6. Appendix A

Page from DARPA web site as of November 8, 2002



R&D PROJECTS

DARPA Special Projects Office

Micro-Electromechanical Sensor (MEMS) Inertial Navigation System (INS)

Program Manager - *Lt Col Gregory Vansuch*

Program Description The Microelectromechanical Sensor Inertial Navigation System (MEMS INS) program will improve the silicon based inertial sensors (gyros and accelerometers) developed in the MEMS technology program and integrate them with navigation software into a low power, small, light weight, low cost, tactical grade INS. In addition to handheld applications, the MEMS INS will be generic for insertion/embedding into other military systems. MEMS INS Phase 1 performed the following: (1) design and development of higher performance MEMS inertial gyroscope and accelerometer sensors; (2) selection and refinement of foundries/foundry processes; (3) design of the mechanical subsystem, and (4) selection/refinement of the navigation software. Phase 2 will develop the MEMS inertial sensors brass board, integrate them into a MEMS INS and demonstrate the brass board in 2002.

For more information about this program, email Lt Col Greg Vansuch at gvansuch@darpa.mil.

[Overview Presentation](#) • [Overview](#) • [R & D Projects](#) • [Personnel](#) • [Solicitations](#) •
[Related Links](#) • [Helper Applications](#) • [Contact SPO](#)

7. Distribution

INTERNAL

5	MS	0501	Andrew Cox, 02334
1		0501	Doug Jordan, 02338
1		0501	Stewart Kohler, 02334
6		0501	Ragon Kinney, 02334
1		0501	Jeffrey Spooner, 02338
1		0503	David Plummer, 02330
1		0509	Michael Callahan, 02300
1		0525	Kurt Wessendorf, 01732
1		0525	Randy Williams, 01732
1		0601	Gregory Peake, 01742
1		0603	Charles Alford, 01742
1		0603	Terry Hargett, 01742
1		0603	Betty Salters, 01742
1		0603	Charles Sullivan, 01742
6		0603	Allen Vawter, 01742
6		0603	Walter Zubrzycki, 01742
1		1071	Michael Knoll, 01730
2		1073	Michael Daily, 01738
3		1073	James Hudgens, 01738
1		1077	Thomas Zipperian, 01740
1		1079	Marion Scott, 01700
1		1425	Stephen Martin, 01707
1	MS	9018	Central Technical Files, 08945-1
2		0899	Technical Library, 09616
1		0612	Review & Approval Desk, 09612
			For DOE/OSTI

**This Page is Inserted by IFW Indexing and Scanning
Operations and is not part of the Official Record**

BEST AVAILABLE IMAGES

Defective images within this document are accurate representations of the original documents submitted by the applicant.

Defects in the images include but are not limited to the items checked:

- ☐ BLACK BORDERS
- ☐ IMAGE CUT OFF AT TOP, BOTTOM OR SIDES
- ☒ FADED TEXT OR DRAWING
- ☐ BLURRED OR ILLEGIBLE TEXT OR DRAWING
- ☐ SKEWED/SLANTED IMAGES
- ☐ COLOR OR BLACK AND WHITE PHOTOGRAPHS
- ☐ GRAY SCALE DOCUMENTS
- ☐ LINES OR MARKS ON ORIGINAL DOCUMENT
- ☐ REFERENCE(S) OR EXHIBIT(S) SUBMITTED ARE POOR QUALITY
- ☐ OTHER: _____

IMAGES ARE BEST AVAILABLE COPY.

As rescanning these documents will not correct the image problems checked, please do not report these problems to the IFW Image Problem Mailbox.